Applied Materials Today 22 (2021) 100932

Contents lists available at ScienceDirect

Applied Materials Today

journal homepage: www.elsevier.com/locate/apmt

Ultralong phase-correlated networks of plasmonic nanoantennas coherently driven by photonic modes

Seyed M. Sadeghi [a,*], Rithvik R. Gutha [b]

[a] Department of Physics and Astronomy, University of Alabama in Huntsville, Huntsville, Alabama 35899, USA
[b] Department of Physics and Astronomy, Living Systems Institute, University of Exeter, Exeter EX4 4QD, United Kingdom

ARTICLE INFO

Article history:
Received 21 October 2020
Revised 25 December 2020
Accepted 29 December 2020

ABSTRACT

We study coherently-stimulated plasmonic dipoles and their phase-correlated coupling, offering ultralong coherent networks of metallic nanoantennas. This is done by considering Au nanoislands with random sizes and shapes placed in close vicinity of each other in a strip with long length and nanoscale width. The positions of the nanoislands in such a strip fluctuate, forming a one-dimensional disordered array. We demonstrate that once such a structure is periodically repeated such that the Rayleigh anomaly condition is satisfied, the photonic lattice modes can drive the plasmon modes of the nanoislands at frequencies dictated by such modes. This allows the nanoislands to act as nano-scale antennas that are excited in phase and are coupled to the neighboring nanoantennas coherently over distances far larger than the sizes of the individual nanoislands. Under these conditions the disordered array acts as a network wherein coherent specifications are distributed in scales far longer than those of the individual nanoislands.

© 2021 Elsevier Ltd. All rights reserved.

Transport of energy and information along certain paths in nanostructure systems in the length scale that is relevant to the device applications are fascinating concepts with many applications. In such systems instead of electrons or photons one deals with the transport of electromagnetic or excitation energy[1–3] In recent years, in particular, intense efforts have been devoted to study transport of energy across metallic nanoparticle (MNP) waveguides. The key feature here is to convert light into plasmonic modes of the MNPs in the presence of their near field coupling [2,4–8]. The common practice is application of chains of MNPs close to each other (Fig. 1a), or formation of arrays of metallic nanoantennas formed via e-beam lithography [9]. Recently impact of retardation in the dispersion and propagation of plasmons of such MNP chains have been investigated [10]. Integration of these chains with dielectric waveguides and optical nano-micro systems have also received significant attentions [11–15]. These investigations also include near infrared waveguides composed of a semi-disordered array of MNPs that can present less loss than micro strip channel waveguides [16].

The current research of plasmonic MNP waveguide structures are mostly based on intrinsic localized surface plasmonic resonances (LSPRs) of MNPs (Fig. 1a) [2,4–7]. In this paper we explore lattice-mode stimulated dipoles in such MNP structures and demonstrate how their coherent coupling offers phase-correlated chains of nanoantennas along distances far longer than the sizes of individual MNPs. For this, instead of one disordered array of MNPs as shown in Fig. 1a, we consider the primary array (P) is supported by several auxiliary structures (A) containing similar structural features (Fig. 1b). The spacings between P and A arrays (a_y) are adjusted such that they support photonic lattice modes (PLMs) at frequencies different than those of the LSPRs of the MNPs. We demonstrate that hybridization of such modes with the disordered MNP arrays can drive plasmons dipoles at frequencies similar to those of PLMs. These dipoles are coherently excited and are in-phase with the incident light. Our results show such plasmonic dipoles can couple to each other coherently across the length of the P waveguide, forming a coherent network consisting of many nanoantennas.

In this paper we study collective resonances in long arrays of Au nanoislands (NISs), exploring the possibility of formation of coherent one-dimensional plasmonic networks (Fig. 1b). To provide a deeper understanding of the impact of PLMs and their relation with the type of metallic nanoantennas (mANTs), we investigate three unique cases. These include (i) long nanorods (NRs) in close proximity of each other from their ends (Fig. 2a), (ii) periodic arrays of mANTs supporting distinct LSPRs with large polarization in the visible range (Fig. 2b), and (iii) periodic disordered arrays of NISs (Fig. 2c). Our results show that in structure (c) each NIS can

* Corresponding author.
E-mail address: seyed.sadeghi@uah.edu (S.M. Sadeghi).

https://doi.org/10.1016/j.apmt.2020.100932
2352-9407/© 2021 Elsevier Ltd. All rights reserved.

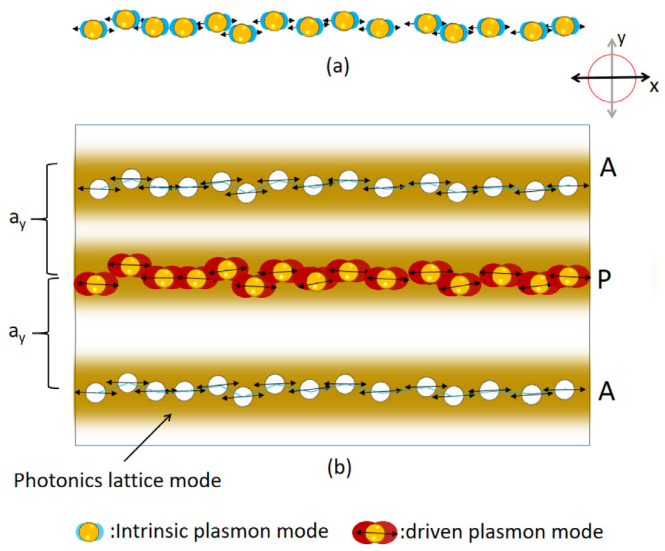

Fig. 1. Disordered arrays of MNPs along one dimension. (a) refers to the case of a disordered array interacting with a light with frequency close to the LSPRs of the MNPs and polarized along x-axis. (b) represents the case wherein such a disordered array (P) is accompanied by several similar arrays (A) with a period of a_y.

act a coherent plasmonic relay post that is coupled to their neighboring posts coherently via optical diffractive modes (Fig. 1b). Because of their relatively small sizes, such NISs do not have large plasmonic polarization, individually.

The photonic lattice modes discussed in this paper are related to surface lattice resonances (SLRs), happening in periodic arrays of mANTs [17–20]. Such resonances occur when Rayleigh Anomaly (RA) condition is satisfied, allowing coherent coupling of LSPRs with the diffraction modes of the lattice. The unique features of SLRs, including their narrow optical features, have made them unique hosts for investigation of excitonic laser systems [21–23], optical filters [24], control of emission of quantum emitters [21,23], perfect absorbers [25], Rabi splitting [26,27], and biological and chemical sensors [28–34]. In a recent report, we showed that SLRs can also happen in the presence of grains or NISs of Au when the are packed together in regions that are periodically repeated in form of two-dimensional lattices[35].

The nanostructure samples studied in this paper were fabricated using electron-beam lithography using Zeiss LEO 1550 SEM (scanning electron microscope). This technique was used to form templates (masks) consisting of periodic arrays of open areas with lattice constants of a_x and a_y along the x- and y-axes, respectively, on glass substrates. The lengths (L) and widths (W) of the open areas were adjusted based on the type of nanostructure samples. In the case of sample 1 (NRs) we considered a_x=2.3 and a_y=0.5 μm, and the values for L and W were set to 2 m and 170 nm, respectively (Fig. 2a). For the case of sample 2, $a_x = a_y = 0.5\mu$m and their L and W, were, respectively, ~220 and ~130 nm (Fig. 2b). For samples 3 and 4, the e-beam masks included long strips of open areas with nominal widths of 200 nm along the x-axis. The separations between the strips (a_y) for these samples were considered to be 500 nm. For the case of samples 1 and 2, we added 2 nm of Cr before placing the e-beam masks. After these steps, layers of Au were evaporated on the top of the masks (CVC Vacuum Evaporation System). For the cases of samples 1 and 2 the thicknesses of the Au layers were 50 nm. In the case of the sample 3 (disordered array of NISs) the mass thickness of the Au layer was 10 nm, and for the case of sample 4, it was slightly higher. As discussed in detail in Ref. [36], the sizes and shapes of the NISs strongly depend on the mass thicknesses of the Au layer. Larger mass thicknesses make the NISs larger and irregular, while smaller mass thicknesses make them more uniform in terms shapes and sizes. After lift-up, samples 1 and 2 were annealed for 5 min at 500 C° and for samples 3 and 4 the annealing temperature and time were 530 C° and 5 min, respectively. We used a transmission setup consisting of a halogen lamp, polarizer, microscope objective, collective lens, and a spectrometer (Ocean Optics TE-cooled QE-pro) to measure extinction spectra of these samples. These spectra were measured when the superstrate medium was either air or methanol. The incident light was considered to either polarized along the x-axis (x-pol) or y-axis (y-pol).

As seen in Fig. 3a, when the polarization of the light is along the x-axis (x-pol) the extinction spectra of sample 1 include several small peaks (solid line). When the refractive index of the superstrate is increased to about 1.33 by adding methanol, these peaks are red shifted, indicating their plasmonic nature (dashed line). When polarization of the incident light is along the y-axis (y-pol), however, the results include a distinct asymmetric peak at 595 nm (Fig. 3a′). This peak is shifted to 655 nm when methanol is added (dashed line). This happens as a secondary peak emerges at about 720 nm (arrow). The main peak here can be associated with the transverse plasmonic modes of the NRs, while the secondary peak (arrow) may be due to the residue of a parallel SLR.

The results of the measurements of the extinction of sample 2 are shown in Figs. 3b and 3b′. For x-pol the results show a dominant peak at 921 nm (Fig. 3b). This peak is associated with the longitudinal plasmon modes of the mANTs. Such a peak shifts to 969 nm and its amplitude decreases as the refractive index of the superstrate increases (dashed line). For y-pol, however, in addition to a small hump around 625 nm, a peak at about 768 nm is generated (Fig. 3b′, solid line). In the presence of methanol, the spectrum changes significantly, resolving a peak at 645 nm and a sharp peak at about 789 nm (dashed line). The sharp peak is an indication of SLR, as will be discussed further in the following.

The results for sample 3 offer a different picture. In this case of x-pol and in the absence of methanol, i.e., when the superstrate is air, we mostly observe a highly asymmetric peak with a ma-

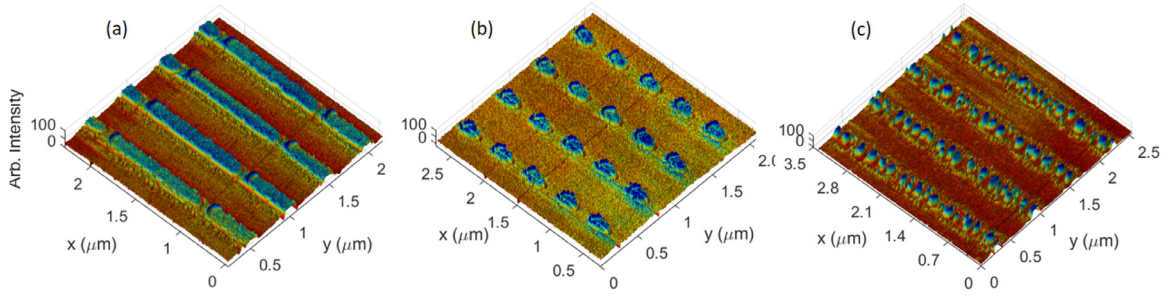

Fig. 2. Oblique SEM images of arrays of Au metallic nanorods (a), mANTs with LSPRs in the visible and near infrared range (b), and long strips containing NISs with random locations, sizes, and shapes (c).

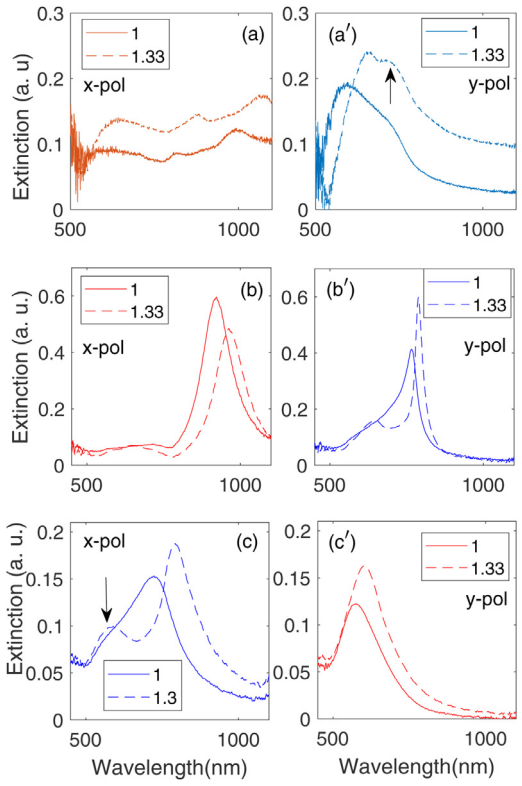

Fig. 3. Extinction spectra of samples 1–3 (structures shown in Figs. 2a-2c) for x-pol (a-c) and y-pol (a′-c′) when the superstrate is air (solid lines) and methanol (dashed lines).

jor peak at about 722 nm (Fig. 3c, solid line) and a hump at about 575 nm (arrow). As the refractive index of the superstrate increases (adding methanol), this peak shifts to 793 while its amplitude increases (dashed line). This process resolves another peak at 584 nm. For y-pol, however, the results for sample 3 show a single peak at about 577 nm (Fig. 3c′, solid line). Addition of methanol shifts this peak to 616 nm, while its amplitude increases (dashed line).

To further explore these results, we consider sample 4, which is similar to sample 3 but with larger and more packed NISs (Fig. 4a). We also consider the optical responses of a reference sample containing NISs similar to those in Fig. 4a, but without any periodicity (Fig. 4c). The extinction spectra of the structure in Fig. 4a are shown in Fig. 4b. The results are similar to those presented in Fig. 3a for sample 3, but with better resolved peaks. In this figure lines 1 and 2 refer to the extinction spectra for x-pol when the superstrate is air and methanol, respectively. Lines 1′ and 2′ are the corresponding spectra when the incident light was polarized along y-axis (y-pol). The results for the structure shown in Fig. 4c, however, closely follow those presented for y-pol in the cases of samples 3 and 4 (Fig. 4d). These results further highlight the fact that in samples 3 and 4 for y-pol there is no optical interaction between PLMs and NISs. In fact in these cases the responses of the arrays are mostly associated with single NISs, as indicated by the results presented in Fig. 4d.

To understand these results we used finite difference time domain (FDTD) to numerically analyze the mode properties of the structures considered in this paper . For this we used MultiPhysics simulation suite of Lumerical software (2020a). We start with the case of sample 2, wherein the results suggested formation of SLR and, therefore, hybridization of LSPRs with RA. Fig. 5a shows the structure file considered for simulation. For this structure we considered the substrate refractive index is 1.45, as of glass, and the refractive index of the superstrate was either 1 (air) or 1.33. Similar to experimental set up, the incident light reached this structure normal to its plan along the z axis and was polarized along the x- or y-axes. We probed the transmittance (T) of this structure and then calculated extinction as 1-T. The meshing size was considered to be 2 nm.

The simulation results for the extinction are shown in Fig. 5b. These results suggest a fairly good match with the experimental results presented in Fig. 3b and 3b′. As seen in Fig. 5b, this includes formation of a dominant peak for x-pol which with increase of refractive index it is red shifted (lines 1′ and 2′). The mode field enhancement profiles, defined as the ratio of field intensity in the presence of mANTs arrays to that in their absence, of these peaks are shown in the Supporting Information (Fig. S1). These results show that for x-pol the mode profiles mostly follow the LSPR responses of individual mANTs.

For the case of y-pol, the results of simulation for extinction are presented in Fig. 5b (lines 1 and 2). When the superstarte is air, we see an asymmetric peak (line 1), similar to the results presented in Fig. 3b′ (solid line). Increase of the refractive index to 1.33 leads to formation of a sharp peak at 755 nm and a shorter wavelength peak at about 650 nm (Fig. 5b, line 2). The modal field enhancement profiles associated with the peak at ~650 nm suggests excitation of LSPRs (Fig. 5c-5e). In the case of the sharp peak at 755 nm, however, the situation is rather different. Fig. 5c′-5e′ show the mode field enhancement profiles associated this peak in the x-y, x-z, and y-z planes, respectively. The x-y plane passes through the middle of mANTs, parallel to the plane of the array. The x-z and y-z planes, other the hand, are perpendicular to this plane but they are along the x- and y-axes, respectively. The results in Fig. 5c′-5e′ suggest that in addition to fields associated with LSPRs, there are signatures of photonic lattice modes (PLMs) in both substrate and superstrate. Coupling of such modes with LSPRs leads to formation of SLR.

To further discuss the process of SLR formation, note that the Rayleigh anomaly (RA) wavelength is given by $\lambda_{RA} = \frac{n}{m}a$. Here n is the refractive index of the substrate (n_{sub}) or superstrate (n_{sup}), m is the diffraction order, and a is the lattice constant (a_x or a_y). When the refractive index of the superstrate is 1.33, the RA wavelength for optical diffraction in superstarte is 665 nm. On the other hand, the RA wavelength for such a process in the substrate is about 725 nm. The results in Fig. 5e′ suggest that optical coupling of LSPRs can occur mostly inside the substrate. This supports a SLR which is consistent with the results presented in Fig. 5b (line 2), and with the fact that this resonance is more efficient in homogenous media [37]. When the superstrate is air the SLR is not mature (Fig. 5e, line 1) [18]. Note that for x-pol (Fig. 3b), we did not see any signature of SLR, since the longitudinal LSPRs of the mANTs in sample 2 were far in the longer side of the RA wavelength.

To discuss the results presented in Fig. 3c and 3c′, we carried out simulation considering the structures as shown in Fig. 6a-6c. These structures include strips containing random distributions of Au nanospheres with minimum and maximum radii of 10 and 50 nm in regions with different width (W) separated from each other by a_y=500 nm. The size distribution of the nanospheres is more or less similar to that of the NIS in sample 3, although it does not include shape variations as seen in this sample. Considering the sizes of NISs are small, however, we do not expect this has significant impact on the results. Fig. 5a and 5b depict structures where W=50 and 200 nm, respectively. We also consider the case of W=100 nm. Fig. 5c shows a close-view of the nanosphere distribution for the case with W=200 nm. The heights of the regions (strips) containing the nanospheres are considered to be 100 nm. This value is imposed by the fact that we consider the maximum radius of the Au nanospheres to be 50 nm. Such spheres have projected sizes of 100 nm for the incident light, which fairly match with the experimental values for the upper range sizes of the

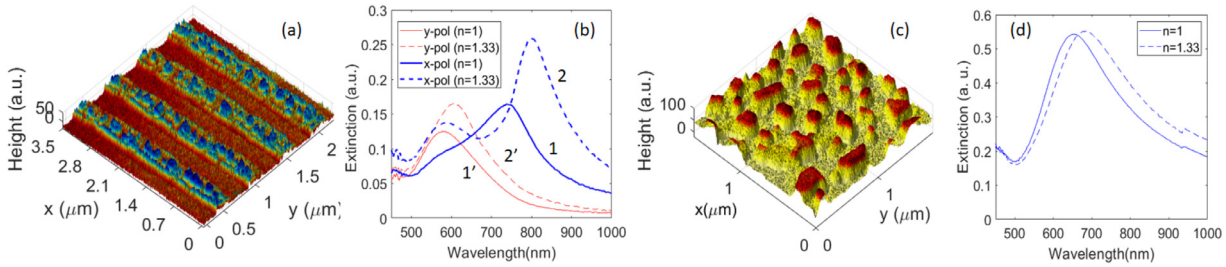

Fig. 4. (a) SEM image of sample 4, (b) extinction spectra of this sample for x-pol (lines 1 and 2) and y-pol (lines 1′ and 2′), (c) the SEM image of a reference sample with similar NISs but without periodicity, (d) extinction spectra of this sample. In (d) the solid line refers to the case when the superstrate was air ($n_{sup} = 1$) and the dashed line to the case when it was methanol ($n_{sup} = 1.33$).

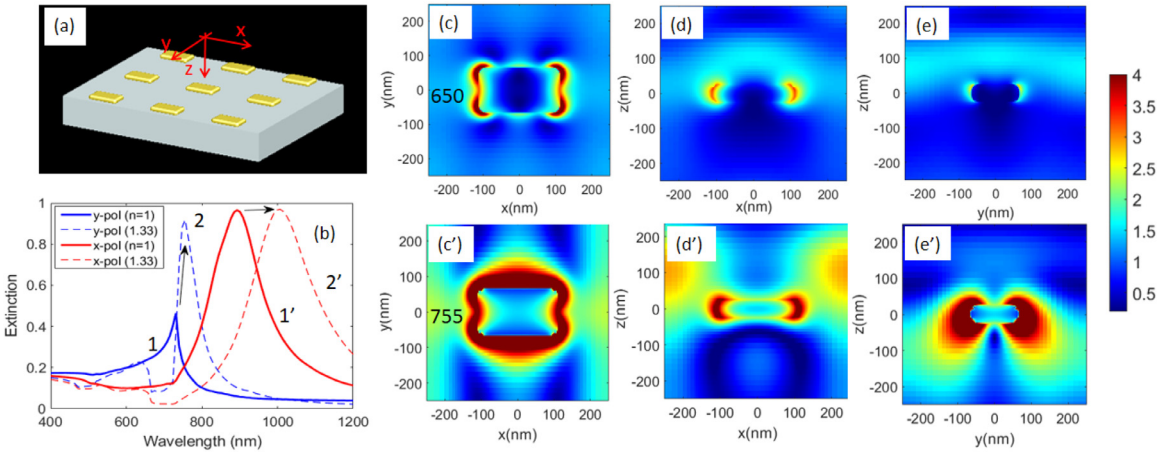

Fig. 5. (a) Simulation structure that replicates sample 2. (b) Simulation results for the extinction of such a structure when the superstrate is air (lines 1 and 1′) and methanol (lines 2 and 2′). Lines 1 (1′) and 2 (2′) refer to the case when the incident light is polarized along the y-axis (x-axis). (c)-(e) show the field enhancement profiles at 650 nm in the x-y, x-z, and y-z planes, respectively, when the incident light is polarized along the y-axis and the refractive index of superstrate is 1.33. (c′)-(e′) represent the mode profiles of the same case as that of (c)-(e), respectively, but at 755 nm.

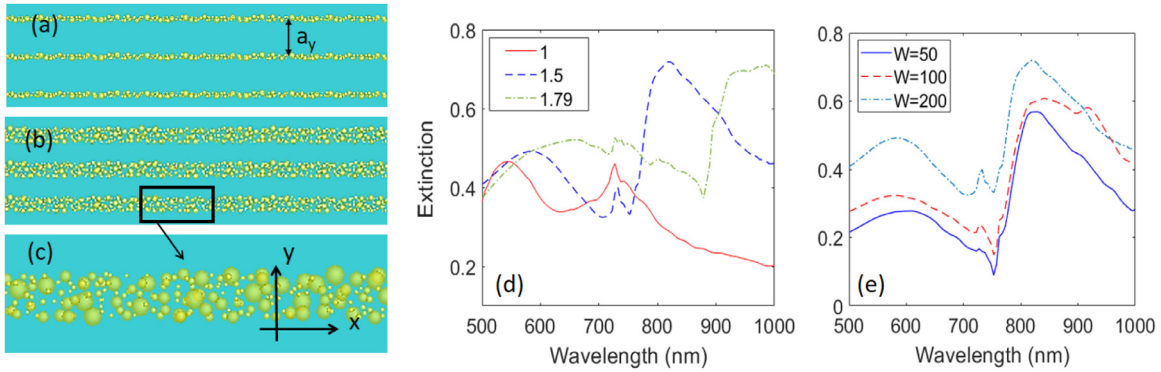

Fig. 6. (a) and (b) show the topviews of the structures used for simulation with W=50 and 200 nm, respectively. (c) presents a closeview of the structure shown in (b). The solid, dashed, and dotted-dashed lines in (d) show the results of simulation for extinction spectra when W=200 and n_{sup}=1, 1.5, and 1.79, respectively. (e) shows the results when n_{sup}=1.5 and W=50 (solid line), 100 (dashed line) and 200 nm (dotted-dashed line). Here H=100, r_{min}=10, r_{max}=50 nm, and the incident light was polarized along the x-axis.

NISs (Fig. 2c). Here we also consider the substrate to have refractive index of 1.45 (as Silica) and the superstrate refractive index is either 1 (air) or 1.5. The incident light is considered to planar wave with polarization along either the x (x-pol) or the y-axis (y-pol).

Fig. 6d shows the results for the case of W=200 nm (Fig. 6b) when n_{sup}=1 (solid line), 1.5 (dashed line) and 1.79 (dashed-dotted line) and the incident light is polarized along x-axis (x-pol). For the case of n_{sup}=1 we mostly see a peak at 540 nm and another peak at 727 nm. For the case of n_{sup}=1.5, the shorter wavelength peak is red shifted to 585 nm and the peak at 727 significantly reduces in amplitude. The main feature here, however, is formation of a dominant peak at 818 nm, which does not exist when n_{sup}=1. As n_{sup} increases to 1.79, we can see a significant shift in such a peak towards longer wavelengths, reaching about 970 nm. Under this condition, the shorter wavelength peak is also shifted to 656 nm. Under these conditions, the feature seen at 727 nm becomes hardly visible. These results indicate that the longer wavelength peak is prominent when the refractive indices of the superstrate and substrate are similar, i.e, the medium is nearly homogeneous. This is clearly consistent with the experimental observations for samples 3 and 4 (Figs. 3c and 4b).

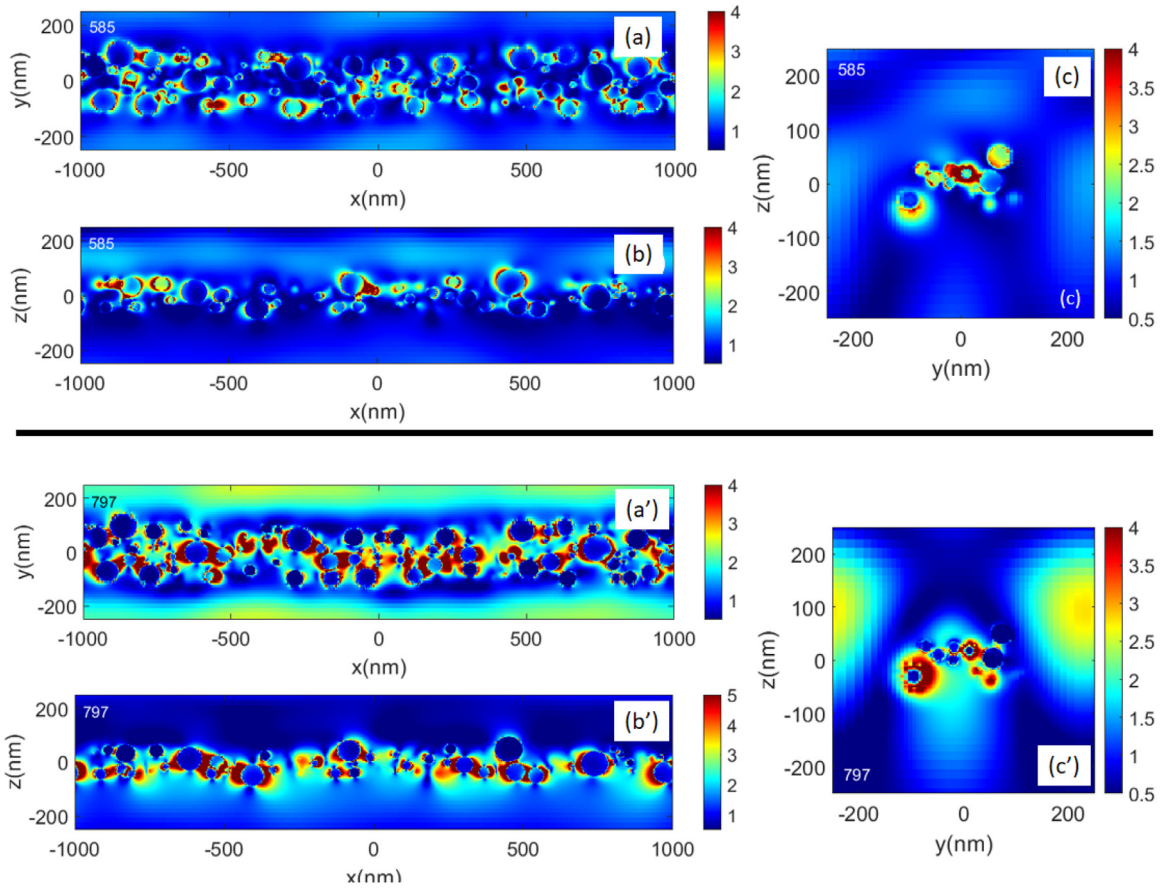

Fig. 7. Modal field enhancement profiles corresponding to the spectrum shown in Fig.7d (dashed line) at 585 (a-c) and 797 nm (a′-c′) in the x-y, x-z, and y-z planes. Here W=200 nm and n_{sup}=1.5.

When the polarization of the incident light is along the y-axis (y-pol), the situation changes dramatically. As seen in the Supporting Information (Fig. S2), under this condition we mostly see a prominent peak at the shorter wavelength range and a feature at 727 nm. For the case of n_{sup}=1 the shorter wavelength peak occurs at 515 nm. For n_{sup}=1.5 this peak shifts to 550 nm. These results indicate that for such a polarization the dominant longer wavelength peak, which happens for x-pol (Fig. 6d), does not exist. Therefore, Fig. S2 more or less supports the experimental results for y-pol (Fig. 3c′), wherein we mostly see optical responses of individual NISs as if the periodicity does not exist. Note that the optical feature seen at 727 nm in Fig. S2 can be associated with the residue of a SLR in the substrate. This feature was not resolved experimentally. Fig. S3 shows the mode field enhancement profiles associated with y-pol at 550 and 727 nm.

Fig. 6e compares the results for the cases of W=50 nm (solid line), 100 nm (dashed line) and 200 nm (dashed-dotted line) for x-pol and n_{sup}=1.5. These results show three main features. The first is related to the wavelengths of the shorter wavelength peaks. In the case of W=50 nm this peak occurs at 611 nm. For W=100 and 200 nm this peak is blue shifted to 585 and 580 nm, respectively. This can be associated with the fact that the number of the nanospheres per unit length (1 μm) of the strips in the case of W=50, 100, and 200 nm are, respectively, 108, 154, 200. Therefore, the wavelength shifts can be an indication of the impact of inter-nanosphere plasmonic coupling. The second feature is related to the small peaks seen at about 727 nm. In the case of W=50 nm, this peak nearly does not exist. As W increases, however, this peak appears and becomes more visible. For this note that since the RA wavelength for optical diffraction in the substrate is 725 nm, this peak can be associated with a SLR caused by orthogonal coupling of the diffraction modes with the LSPRs associated with the shorter wavelength peaks, i.e., at 585 and 580 nm. The third feature seen in Fig. 6e refers to the peaks at about 810 nm and the fact they do not change significantly with W.

To further analyze the results we consider the modal field enhancement factor associated with W=200 nm and n_{sup} =1.5 (Fig. 6d, dashed line). Fig. 7 shows the results at 585 nm (the shorter peak wavelength) in the x-y (a), x-z (b), and y-z (c) planes. At this wavelength the incident field which is polarized along the x-axis excites the intrinsic LSPRs of the individual nanospheres. Since such nanoparticles are close to each other, we can also see some degree of their plasmonic coupling.

Fig. 7 a′-7c′ show the results for the mode profiles for the same structure but at 797 nm, i.e., the longer wavelength peak seen in Fig. 6d (dashed line). Compared to the results shown in Figs. 7a–6c, here we can see much larger field enhancement. Additionally, the coupling between the nanoparticles also becomes stronger. The results also show the presence of PLMs parallel to the disordered nanoparticle array along the x-axis. These modes can be seem clearly in Fig. 7c′, indicating that at this wavelength the nanoparticles have good amount of overlap with the lattice mode, suggesting hybridization. Part of this mode is resided in the substrate, as can also be seen in Fig. 7b′. In addition to these, Fig. 7a′ and 7c′ suggest the presence of two optical modes in the superstrate parallel to nanoparticle array but without any overlap.

Fig. 6e shows that as W becomes smaller the amount of the extinction decreases to some extent. For the shorter wavelength peak happening at ∼ 611 nm, the amount of reduction seems to be more prominent. For the dominant longer wavelength peak,

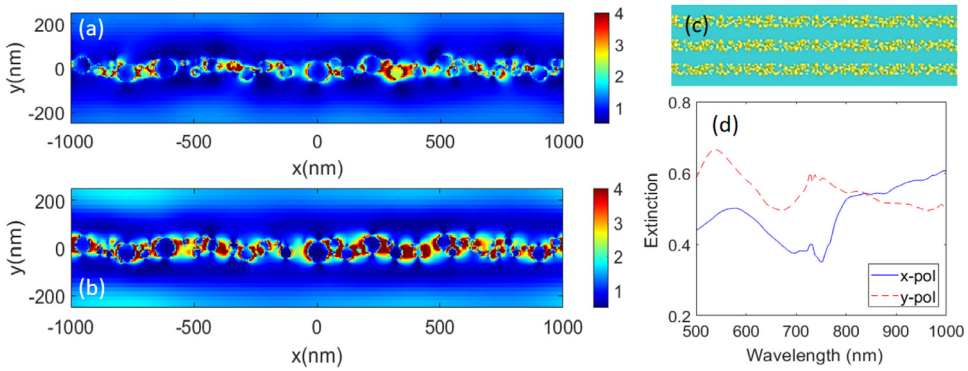

Fig. 8. (a) and (b) the field enhancement factor profiles in the x-y plane at 611 and 828 nm, respectively. (c) shows the topview of the simulation structure with r_{min}=10 and r_{max}=50 nm with allowed overlap between the Au nanospheres. The width of region is considered to be 100 nm and its height is 100 nm. (d) shows the simulation results for the extinction spectra of the structure shown in (c) for x-pol (solid line) and y-pol (dashed line) when n_{sup}=1.5.

which is a sign of collective coupling of nanoparticles, the result suggest a resilient feature. To clarify this further, in Fig. 8a and 8b we show the mode field enhancement profiles at 611 and 828 nm, respectively. Fig. 8b shows how PLM enhances the coupling between narrow disordered array of nanoparticles along the x-axis.

Up to now we considered the cases wherein the MNPs were not touching each other. In the presence of physical contact one expects some changes in the plasmonic properties of the MNPs[7]. To explore the impact of the inter-nanoparticle touching, we considered the case wherein r_{min}=10 and r_{max}=50 nm, as the case considered in Fig. 6b, but allowed the software to include overlap between the MNPs. Under this condition, as shown in Fig. 8c, the Au nanospheres are not necessarily isolated. The results of simulation for extinction of such a structure when n_{sub}=1.5 and W=200 nm are shown in Fig. 8d. For x-pol, in contrast to the result shown in Fig. 6d (dashed line) where we saw a dominant peak at about 800 nm, here the results only show a rise in the extinction at this wavelength without forming a distinct peak (solid line). The results for y-pol (dashed line), however, seem to be fairly similar to those for the structure shown in Fig. 6b (Fig. S2). The field enhancement profiles associated with the x-pol and y-pol cases shown in Fig. 8d are presented in Fig. S4.

The results presented in Fig. 7a'-7c′ suggest formation of a coherent network of Au nanoparticles at the wavelength wherein PLMs overlap with the nanoparticle disordered array (Fig. 7c′). This is quite prominent when W=200 nm, although it also happens when W=50 and 100 nm. These results suggest that the longer wavelength peaks seen in Fig. 3c (and Fig. 4b, line 2) are indications of a coherent network associated with the enhanced coupling between NISs. Such a network becomes efficient when the refractive index of the superstrate is close to that of the substrate, i.e., in homogeneous media. Under these conditions, each isolated NISs in samples 3 and 4 act as a coherent plasmonic relay that is excited by PLMs. Under these conditions, each NIS is driven by PLMs at a frequency that is different than the intrinsic frequencies of the LSPRs of the NISs. When the sizes of NISs are increased, as shown in Fig. 4a, the larger NISs perform more efficiently as coherent nanoantennas in the disordered NIS array. This leads to a more distinct peak at about 800 nm (Fig. 4b, line 2), indicating a stronger collective excitation. The results in Figs. 7 and 8 show that coupling between the stimulated dipoles can extend over ultra-long spatial distances, far larger than the sizes of the individual NISs.

Note that when the disordered NISs arrays were replaced by NRs (Fig. 2a), the outcomes changed dramatically (Fig. 3a and 3a′). The response for x-pol in this case is mostly related to the plasmonic standing waves across the lengths of the NRs. In the case of Fig. 2b, wherein we had an array of mANTs, for y-pol we observed optical features associated with SLR, similar to those seen for the disordered NIS array structure for x-pol. For x-pol in the case of the mANT array (Fig. 2a) we mostly observed excitation of single mANTs. This happened in the case of sample 3 when the light was polarized along y-axis. This can be related to the fact that in the case of structure Fig. 2b, for y-pol the SLR is associated with the orthogonal hybridization of LSPRs with RA [18,38].

In conclusion, we investigated formation of coherent networks of NISs by photonic lattice modes. We demonstrated that at certain wavelengths wherein such modes overlap with the disordered arrays of NISs, they can induce plasmon modes that can efficiently be coupled with the plasmonic modes of other NISs. Since this process was induced by coherent light diffraction, the phase properties of the induced dipoles were the same. Various forms of periodic nanoantennas were investigated and the impact of their shapes and sizes on the coherent coupling of the disordered NISs arrays were explored. The results suggest NISs can offer networks based on coherent excitation and coupling of the induced dipoles. These results may office new avenues for investigation of transport of energy and information.

Data and materials availability: All data needed to evaluate the conclusions in the paper are present in the paper and/or the Supplementary Materials. Additional data related to this paper may be requested from the authors.

Declaration of Competing Interest

The authors declare that they have no known competing financial interests or personal relationships that could have appeared to influence the work reported in this paper.

CRediT authorship contribution statement

Seyed M. Sadeghi: Conceptualization, Methodology, Formal analysis, Visualization, Writing - original draft. **Rithvik R. Gutha:** Data curation, Investigation, Writing - review & editing.

Acknowledgements

This work is supported by the US National Science Foundation under grant ECCS-1917544.

Supplementary material

Supplementary material associated with this article can be found, in the online version, at 10.1016/j.apmt.2020.100932.

References

[1] D.N. Biggerstaff, R. Heilmann, A.A. Zecevik, M. Gräfe, M.A. Broome, A. Fedrizzi, S. Nolte, A. Szameit, A.G. White, I. Kassal, Enhancing coherent transport in a photonic network using controllable decoherence, Nat. Commun. 7 (1) (2016) 1–6.

[2] S.A. Maier, P.G. Kik, H.A. Atwater, Observation of coupled plasmon-polariton modes in au nanoparticle chain waveguides of different lengths: estimation of waveguide loss, Appl. Phys. Lett. 81 (9) (2002) 1714–1716.

[3] K. Boeneman, D.E. Prasuhn, J.B. Blanco-Canosa, P.E. Dawson, J.S. Melinger, M. Ancona, M.H. Stewart, K. Susumu, A. Huston, I.L. Medintz, Self-assembled quantum dot-sensitized multivalent dna photonic wires, J. Am. Chem. Soc. 132 (51) (2010) 18177–18190.

[4] M. Quinten, A. Leitner, J.R. Krenn, F.R. Aussenegg, Electromagnetic energy transport via linear chains of silver nanoparticles, Opt. Lett. 23 (17) (1998) 1331–1333.

[5] S.A. Maier, P.G. Kik, H.A. Atwater, S. Meltzer, E. Harel, B.E. Koel, A.A. Requicha, Local detection of electromagnetic energy transport below the diffraction limit in metal nanoparticle plasmon waveguides, Nat. Mater. 2 (4) (2003) 229–232.

[6] M.L. Brongersma, J.W. Hartman, H.A. Atwater, Electromagnetic energy transfer and switching in nanoparticle chain arrays below the diffraction limit, Phys. Rev. B 62 (24) (2000) R16356.

[7] N.J. Halas, S. Lal, W.-S. Chang, S. Link, P. Nordlander, Plasmons in strongly coupled metallic nanostructures, Chem. Rev. 111 (6) (2011) 3913–3961.

[8] B. Willingham, S. Link, Energy transport in metal nanoparticle chains via sub-radiant plasmon modes, Opt. Express 19 (7) (2011) 6450–6461.

[9] A. Apuzzo, M. Février, R. Salas-Montiel, A. Bruyant, A. Chelnokov, G. Lérondel, B. Dagens, S. Blaize, Observation of near-field dipolar interactions involved in a metal nanoparticle chain waveguide, Nano Lett. 13 (3) (2013) 1000–1006.

[10] C.A. Downing, E. Mariani, G. Weick, Retardation effects on the dispersion and propagation of plasmons in metallic nanoparticle chains, J. Phys.: Condens. Matter. 30 (2) (2017) 025301.

[11] M. Février, P. Gogol, A. Aassime, R. Mégy, C. Delacour, A. Chelnokov, A. Apuzzo, S. Blaize, J.-M. Lourtioz, B. Dagens, Giant coupling effect between metal nanoparticle chain and optical waveguide, Nano Lett. 12 (2) (2012) 1032–1037.

[12] Y. Ma, B. Dong, C. Lee, Progress of infrared guided-wave nanophotonic sensors and devices, Nano Convergence 7 (2020) 1–34.

[13] R. Quidant, C. Girard, J.-C. Weeber, A. Dereux, Tailoring the transmittance of integrated optical waveguides with short metallic nanoparticle chains, Phys. Rev. B 69 (8) (2004) 085407.

[14] G. Magno, M. Fevrier, P. Gogol, A. Aassime, A. Bondi, R. Mégy, B. Dagens, Strong coupling and vortexes assisted slow light in plasmonic chain-soi waveguide systems, Sci. Rep. 7 (1) (2017) 1–11.

[15] B. Dong, Y. Ma, Z. Ren, C. Lee, Recent progress in nanoplasmonics-based integrated optical micro/nano-systems, J. Phys. D Appl. Phys. 53 (21) (2020) 213001.

[16] H. Kim, K. Jung, S.J. Yeo, W. Chang, J.J. Kim, K. Lee, Y.D. Kim, I.K. Han, S.J. Kwon, Long-distance transmission of broadband near-infrared light guided by a semi-disordered 2d array of metal nanoparticles, Nanoscale 10 (45) (2018) 21275–21283.

[17] V. Kravets, F. Schedin, A. Kabashin, A. Grigorenko, Sensitivity of collective plasmon modes of gold nanoresonators to local environment, Opt. Lett. 35 (7) (2010) 956–958.

[18] S.M. Sadeghi, R.R. Gutha, W.J. Wing, Turning on plasmonic lattice modes in metallic nanoantenna arrays via silicon thin films, Opt. Lett. 41 (14) (2016) 3367–3370.

[19] A. Vitrey, L. Aigouy, P. Prieto, J.M. García-Martín, M.U. González, Parallel collective resonances in arrays of gold nanorods, Nano Lett. 14 (4) (2014) 2079–2085.

[20] R.R. Gutha, S.M. Sadeghi, C. Sharp, W.J. Wing, Multiplexed infrared plasmonic surface lattice resonances, J. Phys. D Appl. Phys. 51 (4) (2018) 045305.

[21] R. Guo, S. Derom, A. Väkeväinen, R. van Dijk-Moes, P. Liljeroth, D. Vanmaekelbergh, P. Törmä, Controlling quantum dot emission by plasmonic nanoarrays, Opt. Express 23 (22) (2015) 28206–28215.

[22] M. Ramezani, G. Lozano, M.A. Verschuuren, J. Gómez-Rivas, Modified emission of extended light emitting layers by selective coupling to collective lattice resonances, Phys. Rev. B 94 (12) (2016) 125406.

[23] X. Yuan, L. Shi, Q. Wang, C. Chen, X. Liu, L. Sun, B. Zhang, J. Zi, W. Lu, Spontaneous emission modulation of colloidal quantum dots via efficient coupling with hybrid plasmonic photonic crystal, Opt. Express 22 (19) (2014) 23473–23479.

[24] R.R. Gutha, S.M. Sadeghi, C. Sharp, A. Hatef, Y. Lin, Multi-order surface lattice resonances and dark mode activation in metallic nanoantenna arrays, J. Appl. Phys. 125 (2) (2019) 023103.

[25] N. Liu, M. Mesch, T. Weiss, M. Hentschel, H. Giessen, Infrared perfect absorber and its application as plasmonic sensor, Nano Lett. 10 (7) (2010) 2342–2348.

[26] W. Liu, B. Lee, C.H. Naylor, H.-S. Ee, J. Park, A.C. Johnson, R. Agarwal, Strong exciton–plasmon coupling in MoS2 coupled with plasmonic lattice, Nano Lett. 16 (2) (2016) 1262–1269.

[27] S. Wang, S. Li, T. Chervy, A. Shalabney, S. Azzini, E. Orgiu, J.A. Hutchison, C. Genet, P. Samorì, T.W. Ebbesen, Coherent coupling of WS2 monolayers with metallic photonic nanostructures at room temperature, Nano Lett. 16 (7) (2016) 4368–4374.

[28] R.R. Gutha, S.M. Sadeghi, C. Sharp, W.J. Wing, Biological sensing using hybridization phase of plasmonic resonances with photonic lattice modes in arrays of gold nanoantennas, Nanotechnology 28 (35) (2017) 355504.

[29] X. Zhang, S. Feng, J. Zhang, T. Zhai, H. Liu, Z. Pang, Sensors based on plasmonic-photonic coupling in metallic photonic crystals, Sensors 12 (9) (2012) 12082–12097.

[30] B.D. Thackray, V.G. Kravets, F. Schedin, G. Auton, P.A. Thomas, A.N. Grigorenko, Narrow collective plasmon resonances in nanostructure arrays observed at normal light incidence for simplified sensing in asymmetric air and water environments, ACS Photon 1 (11) (2014) 1116–1126.

[31] B. Auguié, W.L. Barnes, Collective resonances in gold nanoparticle arrays, Phys. Rev. Lett. 101 (14) (2008) 143902.

[32] Y. Sonnefraud, N. Verellen, H. Sobhani, G.A. Vandenbosch, V.V. Moshchalkov, P. Van Dorpe, P. Nordlander, S.A. Maier, Experimental realization of subradiant, superradiant, and fano resonances in ring/disk plasmonic nanocavities, ACS Nano 4 (3) (2010) 1664–1670.

[33] E.M. Hicks, X. Zhang, S. Zou, O. Lyandres, K.G. Spears, G.C. Schatz, R.P. Van Duyne, Plasmonic properties of film over nanowell surfaces fabricated by nanosphere lithography, J. Phys. Chem. B 109 (47) (2005) 22351–22358.

[34] S.M. Sadeghi, W.J. Wing, Q. Campbell, Tunable plasmonic-lattice mode sensors with ultrahigh sensitivities and figure-of-merits, J. Appl. Phys. 119 (24) (2016) 244503.

[35] S.M. Sadeghi, R.R. Gutha, C. Sharp, Coherent optical coupling of plasmonic dipoles in metallic nanoislands with random sizes and shapes, J. Mater. Chem. C 7 (2019) 9678–9685, doi:10.1039/C9TC03351C.

[36] S.M. Sadeghi, R.R. Gutha, W.J. Wing, Impact of the plasmonic metal oxide-induced photocatalytic processes on the interaction of quantum dots with metallic nanoparticles, J. Phys. Chem. C 124 (7) (2020) 4261–4269.

[37] B. Auguié, X.M. Bendana, W.L. Barnes, F.J.G. de Abajo, Diffractive arrays of gold nanoparticles near an interface: critical role of the substrate, Phys. Rev. B 82 (15) (2010) 155447.

[38] V.G. Kravets, A.V. Kabashin, W.L. Barnes, A.N. Grigorenko, Plasmonic surface lattice resonances: a review of properties and applications, Chem. Rev. 118 (12) (2018) 5912–5951.